Journal of Zhejiang University-SCIENCE B (Biomedicine & Biotechnology) *2025 26(4):353-370*
www.jzus.zju.edu.cn; www.springer.com/journal/11585
E-mail: jzus_b@zju.edu.cn

Research Article
https://doi.org/10.1631/jzus.B2300678

Roles of PANoptosis and related genes in acute liver failure: neoteric insight from bioinformatics analysis and animal experiment verification

Tiantian GE[1*], Yao CHEN[1*], Lantian PANG[2], Junwei SHAO[3✉], Zhi CHEN[1✉]

[1]*State Key Laboratory for Diagnosis and Treatment of Infectious Diseases, National Clinical Research Center for Infectious Diseases, National Medical Center for Infectious Diseases, Collaborative Innovation Center for Diagnosis and Treatment of Infectious Diseases, The First Affiliated Hospital, Zhejiang University School of Medicine, Hangzhou 310003, China*
[2]*Department of Infectious Diseases, The Second Affiliated Hospital, Zhejiang University School of Medicine, Hangzhou 310009, China*
[3]*Division of Hepatobiliary and Pancreatic Surgery, Department of Surgery, The Second Affiliated Hospital, Zhejiang University, School of Medicine, Hangzhou 310009, China*

Abstract: Background: PANoptosis has the features of pyroptosis, apoptosis, and necroptosis. Numerous studies have confirmed the diverse roles of various types of cell death in acute liver failure (ALF), but limited attention has been given to the crosstalk among them. In this study, we aimed to explore the role of PANoptosis in ALF and uncover new targets for its prevention or treatment. Methods: Three ALF-related datasets (GSE14668, GSE62029, and GSE74000) were downloaded from the Gene Expression Omnibus (GEO) database to identify differentially expressed genes (DEGs). Hub genes were identified through intersecting DEGs, genes obtained from weighted gene co-expression network analysis (WGCNA), and genes related to PANoptosis. Gene Ontology (GO), Kyoto Encyclopedia of Genes and Genomes (KEGG), protein–protein interaction (PPI) analyses and gene set enrichment analysis (GSEA) were performed to determine functional roles. Verification was performed using an ALF mouse model. Results: Our results showed that expression of seven hub genes (B-cell lymphoma-2-modifying factor (*BMF*), B-cell lymphoma-2-interacting protein 3-like (*BNIP3L*), Caspase-1 (*CASP1*), receptor-interacting protein kinase 3 (*RIPK3*), uveal autoantigen with coiled-coil domains and ankyrin repeats protein (*UACA*), uncoordinated-5 homolog B receptor (*UNC5B*), and Z-DNA-binding protein 1 (*ZBP1*)) was up-regulated in liver samples of patients. However, in the ALF mouse model, the expression of BNIP3L, RIPK3, phosphorylated RIPK3 (P-RIPK3), UACA, and cleaved caspase-1 was up-regulated, while the expression of CASP1 and UNC5B was down-regulated. The expression of ZBP1 and BMF increased only during the development of ALF, and there was no significant change in the end stage. Immunofluorescence of mouse liver tissue showed that macrophages expressed all seven markers. Western blot results showed that pyroptosis, apoptosis, and necroptosis were always involved in lipopolysaccharide (LPS)/D-galactosamine (D-gal)-induced ALF mice. The ALF cell model showed that bone marrow-derived macrophages (BMDMs) form PANoptosomes after LPS stimulation. Conclusions: Our results suggest that PANoptosis of macrophages promotes the development of ALF. The seven new ALF biomarkers identified and validated in this study may contribute to further investigation of diagnostic markers or novel therapeutic targets of ALF.

Key words: Acute liver failure; PANoptosis; Gene Expression Omnibus (GEO); Biomarker; Therapeutic target

1 Introduction

Acute liver failure (ALF) is a lethal liver disease that can occur after exposure to virus, alcohol, drugs, or an autoimmune response, and is characterized by coagulopathy, encephalopathy, and hepatic metabolic dysfunction (Bernal and Wendon, 2013; Stravitz and Lee, 2019). The first period of ALF involves direct interaction between stimuli and hepatocytes, and the secondary host inflammatory response after cell death

✉ Zhi CHEN, zjuchenzhi@zju.edu.cn
Junwei SHAO, sjw507@163.com
* The two authors contributed equally to this work
Zhi CHEN, https://orcid.org/0000-0002-0848-1502
Junwei SHAO, https://orcid.org/0000-0002-7418-0230
Tiantian GE, https://orcid.org/0000-0002-6595-6949
Yao CHEN, https://orcid.org/0009-0002-4717-3147

Received Sept. 19, 2023; Revision accepted Apr. 23, 2024; Crosschecked Apr. 10, 2025

results in organ failure (Khan et al., 2006). Currently, liver transplantation is the only definitive treatment for ALF, indicating that our current understanding of its mechanism is insufficient.

According to the Nomenclature Committee on Cell Death (NCCD), there are two categories of cell death: accidental cell death (ACD) and regulated cell death (RCD) (Galluzzi et al., 2015). ACD is induced by severe insults which are not considered a target for therapeutic intervention because they cannot be modulated or prevented (Green and Kroemer, 2005; Long and Ryan, 2012). In contrast, RCD can be interrupted by means of genetic or pharmacologic intervention targeted to the key components because its process involves molecular regulatory mechanisms, such as apoptosis, necroptosis, pyroptosis, and ferroptosis, coded by genes (Galluzzi et al., 2014, 2015). Although many studies have identified their respective roles in ALF (Schwabe and Luedde, 2018; Wang et al., 2021; Zheng et al., 2022), a growing body of studies has shown extensive molecular crosstalk among these mechanisms rather than being independent of each other, as previously suggested (Kuriakose et al., 2016; Malireddi et al., 2018). Therefore, it is very important to explore the mechanisms involved in the different RCD pathways.

PANoptosis, a new concept proposed by Malireddi et al. (2019), has the characteristics of apoptosis, pyroptosis, and necroptosis, but cannot be represented solely by any one of them. PANoptosis is triggered by the PANoptosome, a multimeric protein complex that integrates the components from other RCD pathways (Malireddi et al., 2019; Christgen et al., 2020). Although initial studies related to PANoptosis involved diseases caused by bacterial or viral infections, subsequent studies have shown that PANoptosis is also present in some tumor and ischemia-related diseases (Karki et al., 2021a; Lin et al., 2022; Nguyen and Kanneganti, 2022; Yan et al., 2023). ALF is caused by cytokine storms generated by an excessive immune response and one of its clinical manifestations is coagulation dysfunction. Both of these features may provide evidence for a possible relationship between PANoptosis and ALF. In this study, we used bioinformatics methods and an animal ALF model to identify the hub genes of PANoptosis in ALF. These results provide important directions for further study of the diagnosis, progression, and targeted therapy of ALF.

2 Methods

2.1 Microarray data

Three sets of ALF-related transcriptome datasets, GSE14668, GSE62029, and GSE74000, were downloaded from the Gene Expression Omnibus (GEO) database (https://www.ncbi.nlm.nih.gov/geo). Fig. 1 depicts the study flowchart.

2.2 Grouping setting

We used the transcriptome data of liver donors as a control group, and the transcriptome data of patients with hepatitis B virus (HBV)-associated or acetaminophen (APAP)-induced ALF as the ALF group. Transcriptome data from the normal liver tissues of patients with angioma were excluded due to concerns that angioma might impact the results. We treated specimens from the same patient as independent samples that did not require exclusion or merging, as our study did not involve the patients' clinical information, and the gene expression profiles of these specimens were distinct.

2.3 Data processing and identification of differentially expressed genes

Normalization, $\log_2$ transformation, and merging of the three ALF raw datasets were performed using the "inSilicoMerging" package in R software. The Bioconductor "sva" package was applied to the combined dataset to eliminate batch effects (Leek et al., 2012). The "Limma" package was used to screen the differentially expressed genes (DEGs), with the criterion set as $|\log_2(\text{fold change})|>1.5$ and an adjusted P value of <0.05.

2.4 Weighted gene co-expression network analysis

Initially, we calculated the median absolute deviation (MAD) for each gene based on gene expression profiles. Subsequently, the lower 50% of genes with the smallest MAD values were removed. Next, we used the "goodSamplesGenes" function from the weighted gene co-expression network analysis (WGCNA) package in R software to eliminate outliers from both genes and samples. Additionally, we developed a scale-free co-expression network and identified a β shrinkage parameter value of β=24 following the scale-free topology criterion. Lastly, genes exhibiting similar expression patterns were grouped into modules using the

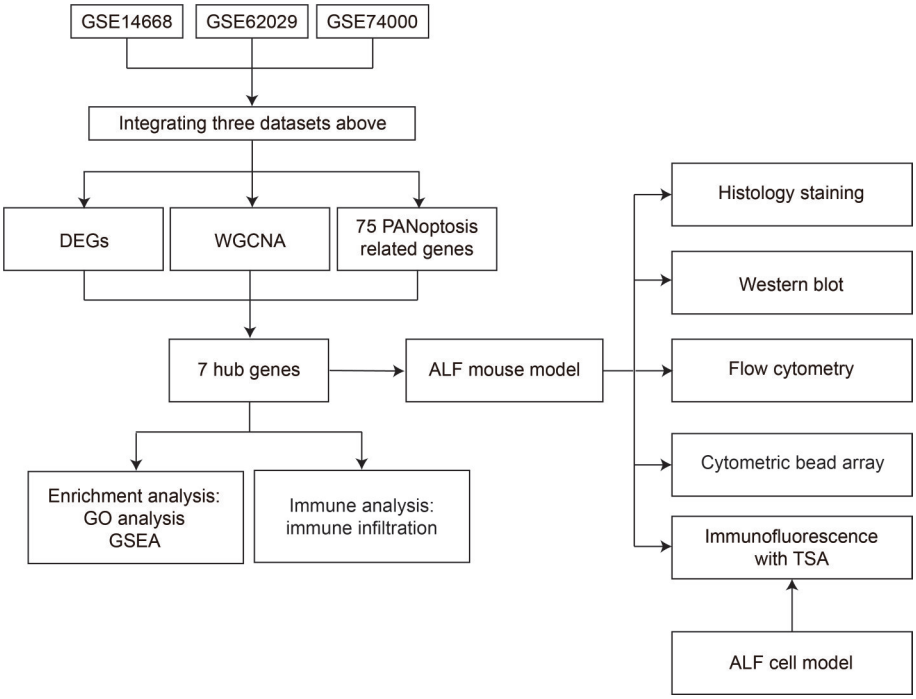

Fig. 1 Flow diagram of the study process. DEGs: differentially expressed genes; WGCNA: weighted gene co-expression network analysis; ALF: acute liver failure; GO: Gene Ontology; GSEA: gene set enrichment analysis; TSA: tyramide signal amplification.

"dynamic tree-cutting" algorithm, and the correlation between sample traits and module genes was assessed through Pearson's correlation analysis.

2.5 Identification of hub genes

The "VennDiagram" package in R software was used to obtain hub genes associated with PANoptosis and ALF by intersecting DEGs, genes obtained from WGCNA, and genes related to PANoptosis. The differences in expression of hub genes between ALF and healthy samples were represented by violin plots. The *t*-test was used for normally distributed data, whereas the Mann-Whitney *U*-test was used for non-normal distributed data. Significance was defined as $P<0.05$.

2.6 Functional enrichment analysis

Gene Ontology (GO) and Kyoto Encyclopedia of Genes and Genomes (KEGG) analyses were carried out to compare the differential signaling pathways and biological effects among the seven genes.

We used the Metascape database (https://metascape.org) for annotation and the Sangerbox database (http://sangerbox.com) for visualization. We set the minimum overlap to 1, since the number of hub genes selected was too small, and the *P* value cutoff was set to <0.05.

2.7 Potential interaction between hub genes

First, we used the STRING database (https://cn.string-db.org) to obtain the interaction relationships among the seven hub genes, and then we gradually expanded the interaction relationship between hub genes until seven genes were connected in a network. Cytoscape (https://cytoscape.org) was then used to remove the non-hub genes whose total number of adjacent hub genes was less than three. The final result was a predicted interaction between hub genes.

2.8 Gene set enrichment analysis

We performed gene set enrichment analysis (GSEA) using GSEA software (version 4.0.3). According to the expression level of target genes, the samples were divided into high-expression group (≥50%) and low-expression group (<50%). The relevant pathways and molecular mechanisms were evaluated based on gene expression profiles and phenotypic grouping by the Molecular Signatures Database (https://www.gsea-msigdb.org). We set the minimum gene set to 5 and the maximum gene set to 5000. A *P* value of <0.05 and a false discovery rate (FDR) of <0.25 were considered statistically significant.

2.9 Analysis of immune infiltration

The abundance of 22 subtypes of immune cells was determined after analyzing the sequencing data of ALF samples using the CIBERSORT algorithm. These subtypes represent the cellular composition of the immune microenvironment in ALF, and Spearman correlation analysis was performed on genes and immune cells.

2.10 Mouse model of ALF

An ALF mouse model was established in randomly assigned 8-week-old C57BL/6 mice (Gampharmatech, Shanghai, China) by intraperitoneal (i.p.) injection of lipopolysaccharide (LPS; 40 μg/kg, Sigma, L4391, Missouri, USA) and D-galactosamine (D-gal; 800 mg/kg, Sigma, G0500) (LPS/D-gal) (Li et al., 2021) after overnight starvation. Control group mice received the same volume of phosphate-buffered saline (PBS). To evaluate the extent of liver injury, liver tissues and serum samples were collected at 0.5, 1, 2, 4, and 6 h after LPS/D-gal injection, while samples of the control group were collected at 6 h after PBS injection. Serum levels of alanine aminotransferase (ALT) and aspartate aminotransferase (AST) were measured using a standard analyzer, DRI-CHEM 4000ie (FUJIFILM, Tokyo, Japan). Cytokine levels in the serum were assessed using the BD Cytometric Bead Array Mouse Inflammation Kit (BD Biosciences, California, USA) and analyzed by flow cytometry.

2.11 Hematoxylin and eosin staining

Liver tissues were fixed in 4% (0.04 g/mL) paraformaldehyde (PFA) and then embedded in paraffin. Sections with a thickness of 5 μm were prepared and subjected to staining with hematoxylin and eosin (H&E).

2.12 Western blot

The liver tissue was cleaved into radioimmunoprecipitation assay (RIPA) buffer containing protease inhibitor and phosphatase inhibitor by a tissue grinder, incubated on ice for 30 min with vortex oscillation once every 10 min, and then centrifuged at 12000*g* for 15 min at 4 °C. After being quantitatively measured by bicinchoninic acid (BCA) solution, the tissue homogenate was boiled in a metal bath at 100 °C for 10 min after being mixed with 5× loading buffer. The mixture was used for western blotting (WB). The antibodies used included B-cell lymphoma-2-modifying factor (BMF; CST, 50542s, Massachusetts, USA), B-cell lymphoma-2-interacting protein 3-like (BNIP3L; CST, 12396T), Caspase-1 (CASP1; Proteintech, 81482-1-RR, Wuhan, China), cleaved caspase-1 (CST, 89332s), cleaved caspase-3 (CST, 9664), cleaved caspase-8 (CST, 8592), glyceraldehyde-3-phosphate dehydrogenase (GAPDH; Proteintech, 60004-1-Ig), gasdermin D (GSDMD; Huabio, er1907-37, Hangzhou, China), gasdermin E (GSDME; Proteintech, 13075-1-AP), goat anti-mouse immunoglobulin G (IgG) (Proteintech, SA00001-1), goat anti-rabbit IgG (Proteintech, SA00001-2), mixed lineage kinase domain-like protein (MLKL; CST, 98110), phosphorylated MLKL (P-MLKL; CST, 98110), phosphorylated receptor-interacting protein kinase 3 (P-RIPK3; CST, 98110), RIPK3 (CST, 98110), uveal autoantigen with coiled-coil domains and ankyrin repeats protein (UACA; Absin, abs119046, Shanghai, China), uncoordinated-5 homolog B receptor (UNC5B; CST, 13851s), and Z-DNA-binding protein 1 (ZBP1; Invitrogen, PA5-20455, California, USA).

2.13 Isolation of liver immune cells

In brief, the liver tissue was shredded by tweezers in digestive fluid containing type IV collagenase and DNase, and then transferred to a constant temperature shaker at 37 °C for further digestion. Next, the liver tissue suspension was filtered with a 70-μm filter. The filtrate was used to precipitate liver cells at a centrifugation rate of 50*g*, and the supernatant containing immune cells was precipitated at a rate of 500*g*. Finally, the immune cells were precipitated by centrifugation in 33.3% Percoll working solution. The immune cells were washed with PBS for subsequent flow cytometry analysis.

2.14 Flow cytometry

A BD LSRFortessa™ (BD Biosciences) cell analyzer was used for flow cytometry. The following fluorescent antibodies were used: anti-CD45-FITC (BioLegend, 103108, California, USA), anti-CD11b-Allophycocyanin (APC) (BioLegend, 101212), anti-F4/80-BV421 (BioLegend, 123131), and anti-7-aminoactinomycin D (7AAD)-APC/cyanine 7(Cy7) (BioLegend, 420404).

2.15 Immunofluorescence with tyramide signal amplification

The paraffin-embedded sections were dewaxed and treated for antigen retrieval, and the endogenous peroxidase was removed with 3% (volume fraction) hydrogen peroxide. Next, each antigen was stained with primary and secondary antibodies, and the signal was amplified with fluorescent staining of different channels according to the instructions. Finally, the nuclei were labeled with 4',6-diamidino-2-phenylindole (DAPI). Antibodies used for immunofluorescence included anti-BMF (QCHENG BIO, QC330Hu01, Shanghai, China), anti-BNIP3L (Proteintech, 68118-1-Ig), anti-CASP1 (Proteintech, 81482-1-RR), anti-RIPK3 (Proteintech, 17563-1-AP), anti-UACA (Proteintech, 25654-1-AP), anti-UNC5B (Huabio, ER1918-41), anti-ZBP1 (Invitrogen, PA5-143928), anti-F4/80 (Proteintech, 29414-1-AP), anti-CD11b (Servicebio, GB115689, Wuhan, China), anti-Ly6C (Servicebio, GB115601), and anti-CASP8 (Proteintech, 66093-1-Ig).

2.16 Verification of the formation of PANoptosomes in the ALF cell model

Bone marrow cells were extracted from the femur and tibia of mice and cultured in Dulbecco's modified Eagle's medium (DMEM), supplemented with 10% (volume fraction) heat-inactivated fetal bovine serum (FBS), 100 U/mL penicillin, 100 μg/mL streptomycin, and 50 ng/mL macrophage colony-stimulating factor (M-CSF). The cells were cultured for three days and then provided with fresh DMEM. Mature bone marrow-derived macrophages (BMDMs) were harvested after seven days of culture and seeded in 12-well glass-bottom plates at 2×10^5 cells/mL in complete DMEM containing 100 mmol/L glutamine. The cells were incubated at 37 °C in a humidified atmosphere with 5% CO_2 overnight for experiments. The following day, the BMDMs were stimulated with LPS (100 ng/mL) for 6 h, followed by immunofluorescence staining using tyramide signal amplification (TSA) for cell imaging.

2.17 Statistical analysis

All data are presented as mean±standard deviation (SD). The Shapiro-Wilk normality test was conducted to assess the normality of the distribution of the data. For comparisons between two groups, an independent samples *t*-test was used. In cases where a normal distribution was not observed, the Mann-Whitney *U*-test was used. In the presence of a normal distribution, one-way analysis of variance (ANOVA) was used to compare three or more groups, followed by Tukey's multiple comparison tests for post-hoc analysis. In instances where a normal distribution was not present, the Kruskal-Wallis test was performed and then a Dunn multiple comparison test was applied for post-hoc analysis. Spearman's rank test was used to evaluate correlations.

3 Results

3.1 Dataset characterization

The GSE14668 dataset had 8 liver specimens obtained from 2 HBV-associated ALF patients, 8 individual liver specimens from 8 liver donors, and 11 normal liver specimens from 11 patients who underwent resection for angioma. GSE62029 had 13 liver specimens obtained from 4 HBV-associated ALF patients, 10 individual liver specimens from 10 liver donors, and 7 normal liver specimens from 7 patients who underwent resection for angioma. GSE74000 had 3 specimens obtained from one APAP-induced ALF patient and 2 healthy livers from individuals deceased from brain damage. All three datasets are from the GPL570 platform (Table 1).

Table 1 Information of three datasets

Name	Etiology	Number				Platform
		ALF patient	ALF sample	Donor	Liver angioma	
GSE14668	HBV	2	8	8	11	GPL570
GSE62029	HBV	4	13	10	7	GPL570
GSE74000	APAP	1	3	1 (2)[&]	0	GPL570

[&] GSE74000 contains one donor, but the donor contributes two samples.
ALF: acute liver failure; HBV: hepatitis B virus; APAP: acetaminophen.

3.2 Identification of DEGs

The intersection of the three datasets is shown in Fig. 2a. Batch effects were removed to obtain the integrated dataset (Figs. 2b–2e). A total of 5113 genes were identified as DEGs using the Limma method, of which 3136 were up-regulated and 1977 down-regulated. A volcano plot and heatmap of the ALF DEGs are shown in Figs. 2f and 2g, respectively.

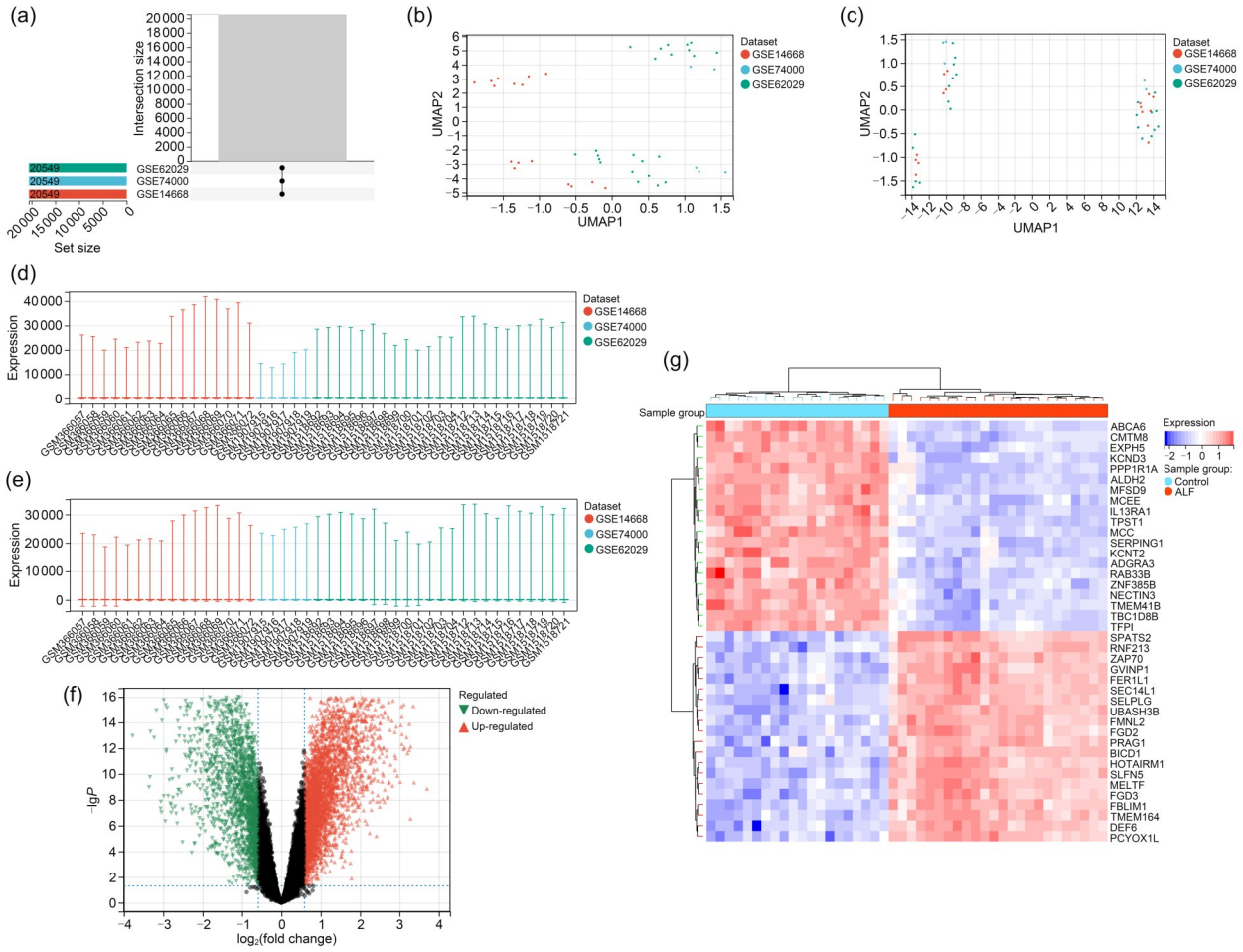

Fig. 2 Screening for differential genes. (a) Intersection sizes of the three datasets. (b, c) Gene expression level statistics of the datasets before and after de-batching. (d, e) Principal component analysis (PCA) of datasets before and after de-batching. (f) Volcano plot of differentially expressed genes (DEGs): up-regulated DEGs are represented by red nodes, down-regulated DEGs by green nodes, and genes with no significant differential expression by black nodes. (g) Heatmap of DEG expression levels: azure indicates control samples, orange indicates acute liver failure (ALF) samples, red indicates high gene expression, and purple indicates low gene expression.

3.3 Weighted gene co-expression network analysis and key module identification

WGCNA was applied to explore the differences in gene expression between the ALF group and the control group. We chose β=24 as the "soft" threshold because it was the first power value when the index of scale-free topologies reached 0.85 (Figs. 3a and 3b). Nine gene co-expression modules (GCMs) discovered based on this power are shown in different colors (Figs. 3c and 3d). The correlation between ALF and GCMs is presented in Fig. 3e. The mediumpurple3 module (1484 genes) was identified as the pivotal module for subsequent analysis since it had the highest correlation with ALF (correlation coefficient r=0.88, P=1.8×10^{-15}). Additionally, a significant positive correlation was observed between gene significance and module membership (correlation coefficient r=0.8) (Fig. 3f). According to the above results, we believe that mediumpurple3 module genes were most significantly associated with ALF.

3.4 Screening and characterization of hub genes

Seven hub genes, namely *BMF*, *BNIP3L*, *CASP1*, *RIPK3*, *UACA*, *UNC5B*, and *ZBP1*, were obtained after intersecting 5113 DEGs, 1484 genes in the "mediumpurple3 module" of WGCNA, and 75 genes related with PANoptosis (*AIFM1*, *AKT3*, *APAF1*, *APPL1*, *BAK1*, *BAX*, *BMF*, *BNIP3L*, *BOK*, *CASP1*, *CASP10*, *CASP2*, *CASP3*, *CASP4*, *CASP5*, *CASP6*, *CASP7*,

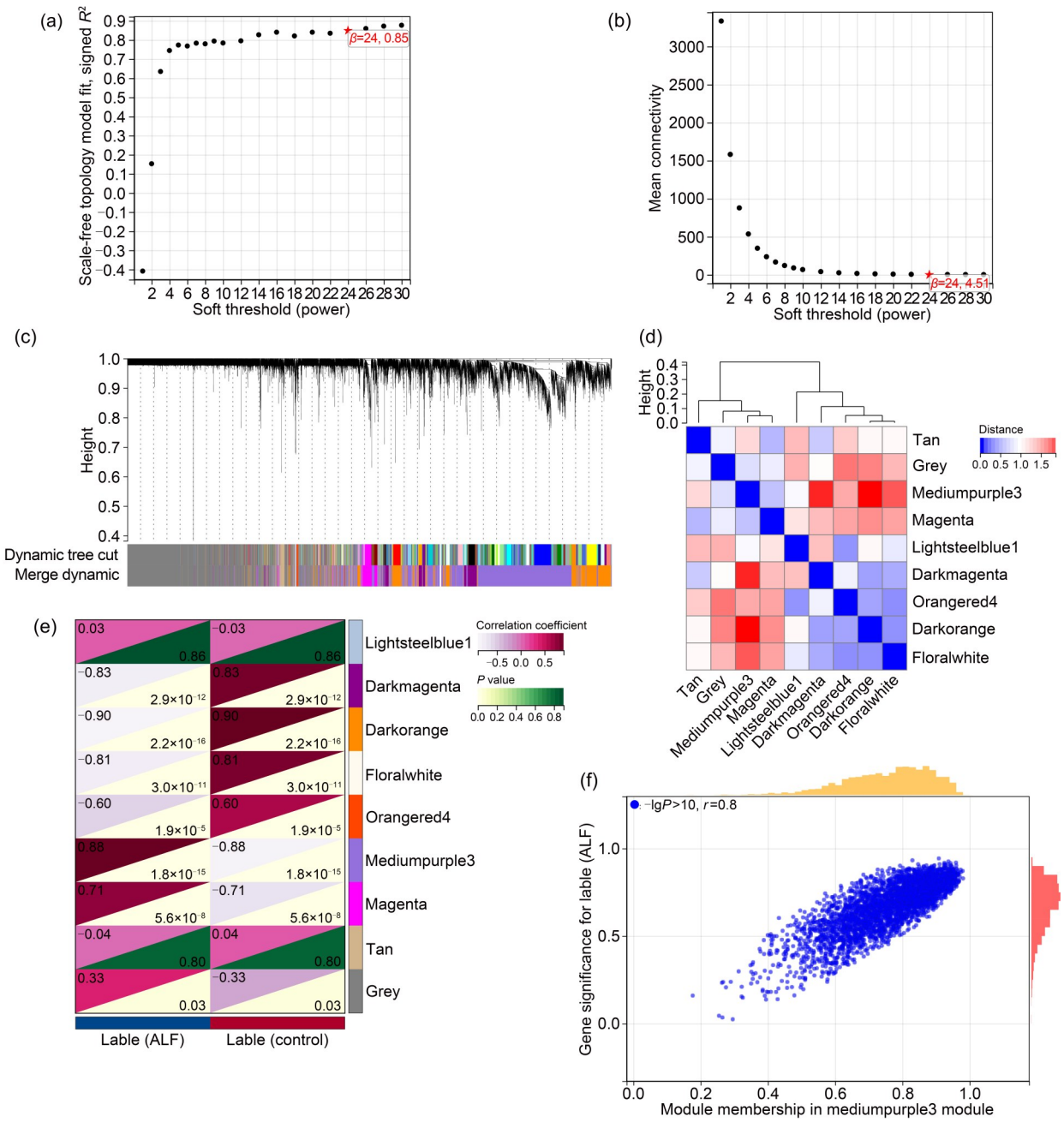

Fig. 3 Weighted gene co-expression network analysis (WGCNA). (a, b) Analysis of the scale-free fit index for various soft-thresholding powers. (c) Gene trees of co-expression gene modules are shown in various colors. (d) Heatmap of eigengene adjacency. (e) Heatmap of the association between acute liver failure (ALF) and modules. The mediumpurple3 module is shown to be significantly correlated with the ALF. The numbers in the top and bottom triangles represent the correlation coefficient and *P* value, respectively. (f) Correlation plot between gene significance and module membership of genes included in the mediumpurple3 module. *r*: correlation coefficient.

CASP8, *CD14*, *CHMP2A*, *CHMP2B*, *CHMP3*, *CHMP4A*, *CHMP4B*, *CHMP4C*, *CHMP6*, *CHMP7*, *CHUK*, *CRADD*, *CYCS*, *DFFA*, *DFFB*, *E2F1*, *ELANE*, *FADD*, *FAS*, *FASLG*, *FLIP*, *GSDMD*, *GSDME*, *GZMB*, *HMGB1*, *HMGB2*, *IGF1*, *IL18*, *IL1A*, *IL1B*, *IRF1*, *IRF2*, *LY96*, *MAP3K7*, *MLKL*, *NLRP3*, *PPP3R1*, *PSTPIP2*, *PYCARD*, *RBCK1*, *RIPK1*, *RIPK3*, *RNF31*, *TFDP1*, *TICAM1*, *TLR3*, *TNFAIP3*, *TNFRSF1A*, *TNFSF10*, *TNF*, *TP63*, *TP73*, *TRAF2*, *UACA*, *UNC5B*, *YWHAE*, *YWHAG*, and *ZBP1*), using the Venn diagram

tool (Fig. 4a). Fig. 4b shows the potential interaction between the seven hub genes. *BCL2L1*, *CASP8*, *CASP9*, and *MLKL* play important roles in this protein–protein interaction network, enabling the seven hub genes to establish interconnections. This further indicates that there is crosstalk among pyroptosis, apoptosis, and necroptosis. Next, GO and KEGG enrichment analyses were performed to reveal the function of PANoptosis-related genes. The PANoptosis-related genes were enriched mainly in pathways involved in the defense response to viruses, positive regulation of hydrolase activity, cytosolic DNA-sensing pathway, regulation of mitochondrion organization, pyroptosis, and positive regulation of the necroptotic process (Fig. 4c). Besides, all hub genes were up-regulated in the ALF group (Fig. 5).

3.5 Gene set enrichment analysis of seven PANoptosis-related genes

To further identify the associated signaling pathways of the seven PANoptosis-related genes, we used GSEA software to perform a single gene differential analysis between the ALF group and the control group. Seven PANoptosis-related genes were positively correlated with part of the signaling pathways, including CELL_ADHESION_MOLECULES_CAMS, CHEMOKINE_SIGNALING_PATHWAY, LYSOSOMEPRIMARY_IMMUNODEFICIENCY, and

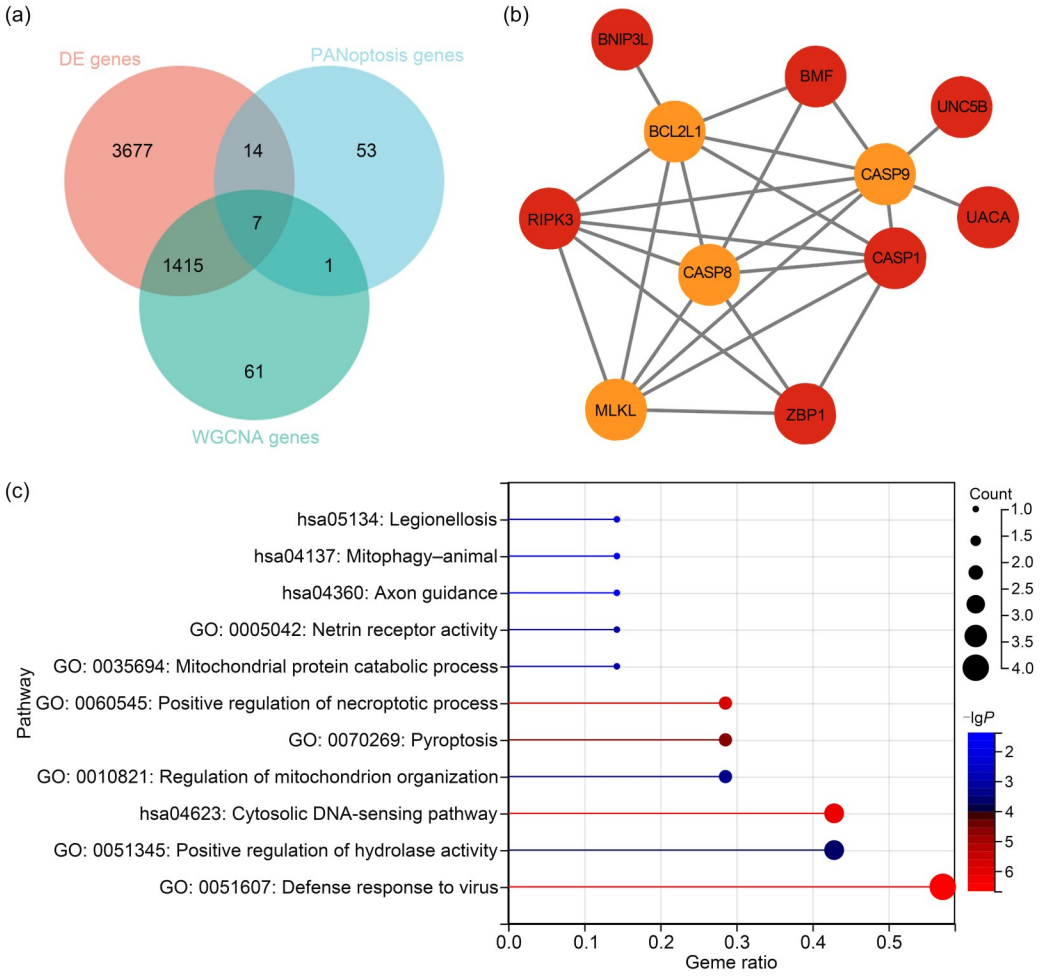

Fig. 4 Selection of the PANoptosis-related genes. (a) Venn diagram showing the seven PANoptosis-related genes from the intersection of DEGs, mediumpurple3 module via weighted gene co-expression network analysis (WGCNA), and 75 genes that refer to PANoptosis. (b) The protein–protein interaction (PPI) network revealed that the seven hub genes were linked directly or indirectly. The genes in the orange circle are the hub genes, and those in the yellow circle are the bridge genes needed to connect the hub genes. (c) Enrichment analyses of Kyoto Encyclopedia of Genes and Genomes (KEGG) and Gene Ontology (GO) pathways related to the seven hub genes.

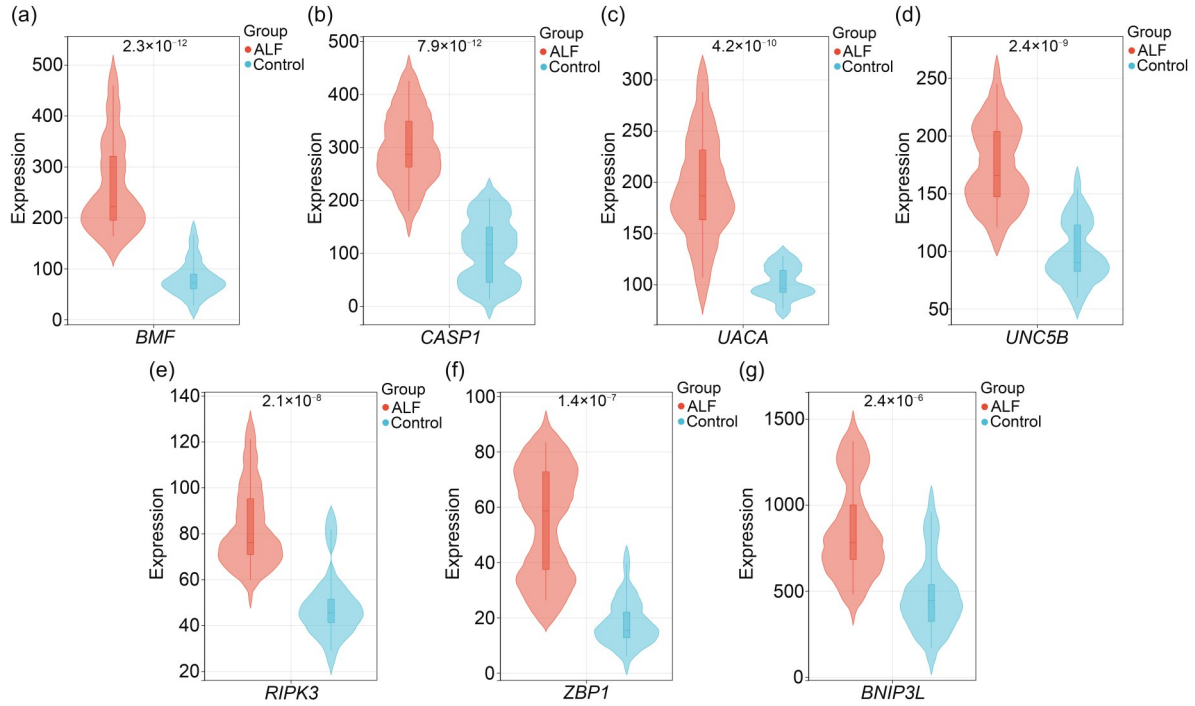

Fig. 5 Violin plots of the expression of seven PANoptosis-related genes in the acute liver failure (ALF) and control groups. (a) Expression of B-cell lymphoma-2-modifying factor (*BMF*). (b) Expression of Caspase-1 (*CASP1*). (c) Expression of uveal autoantigen with coiled-coil domains and ankyrin repeats protein (*UACA*). (d) Expression of uncoordinated-5 homolog B receptor (*UNC5B*). (e) Expression of receptor-interacting protein kinase 3 (*RIPK3*). (f) Expression of Z-DNA-binding protein 1 (*ZBP1*). (g) Expression of B-cell lymphoma-2-interacting protein 3-like (*BNIP3L*). The number at the top of the violin diagram for each gene represents a *P*-value of <0.0001.

ANTIGEN_PROCESSING_AND_PRESENTATION, but negatively correlated with PEROXISOME, except *BNIP3L* (Fig. 6).

3.6 Immune cell infiltration in ALF

CIBERSORT is an appropriate algorithm for investigating the connections between characteristic genes and immune cells. We used CIBERSORT to examine the mechanisms that link feature genes to immune cell infiltration in ALF. The infiltration of immune cells in ALF is depicted in Fig. 7a. Compared with the control group, the ALF group exhibited a significantly higher abundance of memory B cells, CD8 T cells, naive CD4 T cells, T cells, CD4 memory-activated monocytes, and M2 macrophages (Fig. 7c). Furthermore, we explored the association between feature genes and immune cells. Except for *BNIP3L*, the other six PANoptosis-related genes were all negatively associated with activated dendritic cells, activated mast cells, and neutrophils. *BMF*, *CASP1*, *UACA*, and *ZBP1* exhibited a positive correlation with naive CD4 T cells and memory-activated CD4 T cells, while *BNIP3L* showed a positive correlation with only naive CD4 T cells. Also, *BMF*, *CASP1*, and *ZBP1* were negatively correlated with some or all of these immune cells: macrophage infiltration, activated natural killer (NK) cells, and follicular helper T cells (Fig. 7b). These findings indicate that the feature genes are closely linked to immune cell infiltration in the liver and play a critical role in shaping the immune microenvironment in ALF.

3.7 Experimental verification of the ALF mouse model

First, we established an LPS-induced acute liver injury model and observed significant congestion in the livers of mice 6 h after LPS/D-gal injection (Fig. 8a). To investigate the dynamic changes in acute liver injury, we set up different modeling time points. We found that the serum levels of ALT and AST showed no significant changes in mice with early-stage liver failure, but suddenly increased at 6 h, exhibiting a sharp increase (Fig. 8b). Cytokines showed dynamic changes as well. The tumor necrosis factor-α (TNF-α) gradually increased after LPS injection, reaching its peak 1 h after modeling, followed by a gradual decrease. The interferon-γ (IFN-γ) increased only at 4 h

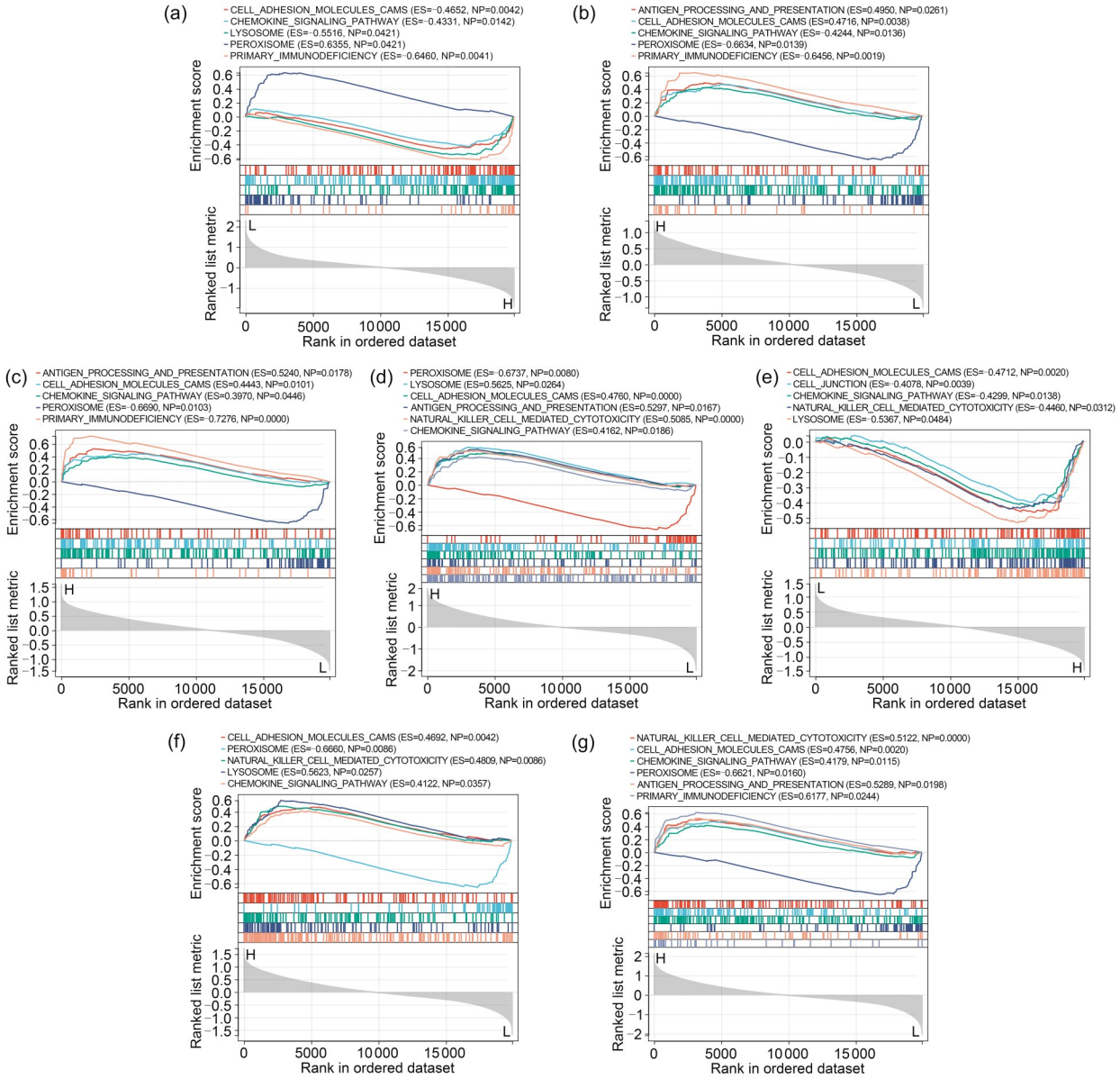

Fig. 6 Gene set enrichment analysis (GSEA) of seven PANoptosis-related genes. (a) GSEA of Caspase-1 (*CASP1*). (b) GSEA of receptor-interacting protein kinase 3 (*RIPK3*). (c) GSEA of Z-DNA-binding protein 1 (*ZBP1*). (d) GSEA of B-cell lymphoma-2-modifying factor (*BMF*). (e) GSEA of B-cell lymphoma-2-interacting protein 3-like (*BNIP3L*). (f) GSEA of uncoordinated-5 homolog B receptor (*UNC5B*). (g) GSEA of uveal autoantigen with coiled-coil domains and ankyrin repeats protein (*UACA*). H represents high-expression group; L represents low-expression group.

after injection, followed by a decrease, while interleukin (IL)-6 peaked 2 h after modeling and then gradually declined. The anti-inflammatory factor IL-10 peaked at 1 h and then gradually decreased.

To explore the dynamic changes of PANoptosis-related genes in the mouse liver, we conducted WB analysis on liver tissue homogenates at various time points. As shown in Fig. 8c, the expression of P-RIPK3, RIPK3, UACA, ZBP1, BNIP3L, and BMF began to increase after LPS injection, but their peak time and change trends were different. The peak expression time of RIPK3 was 0.5 h after modeling while for P-RIPK3 it was 2–4 h, indicating that RIPK3 and its function were activated early on. The peak expression of UACA occurred 4 h after modeling and lasted longer. ZBP1 expression was observed mainly between 0.5 and 2 h. BNIP3L expression gradually increased, peaking at 6 h of modeling, possibly related to ALT and AST expression. The peak expression of BMF occurred at 4 h, but its change amplitude was not significant. UNC5B

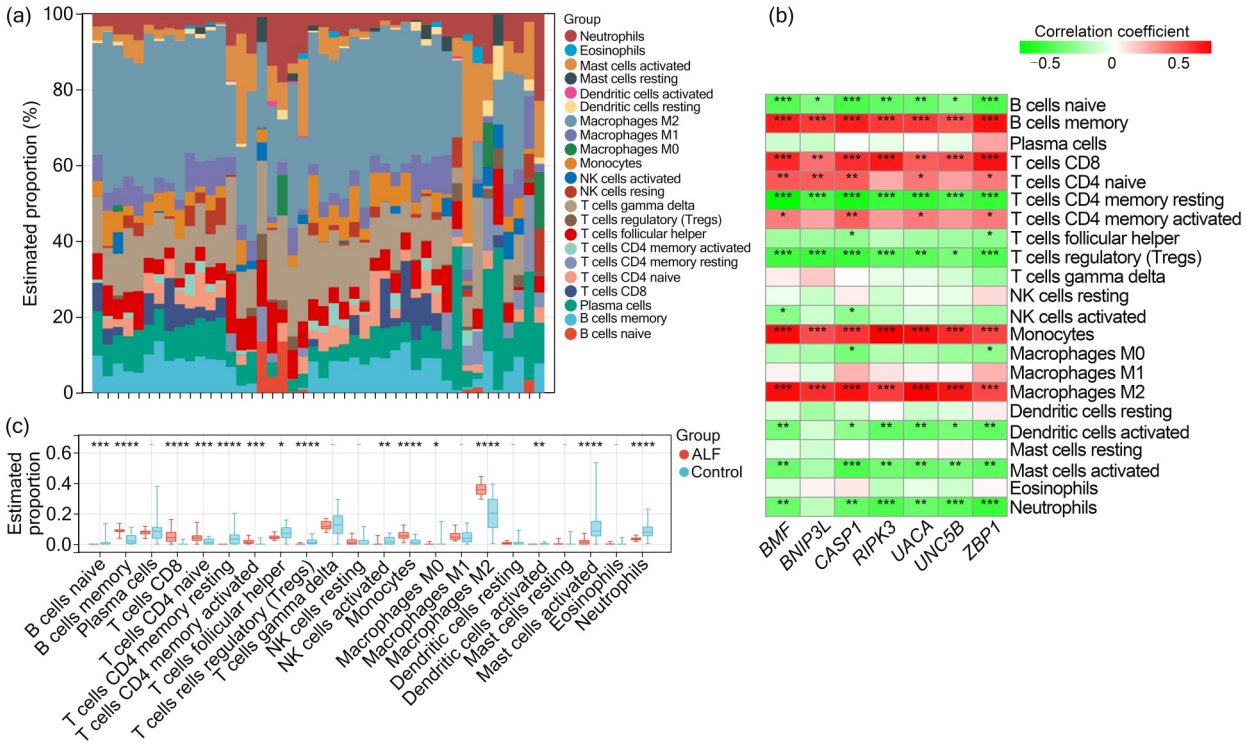

Fig. 7 Immune cell infiltration in acute liver failure (ALF). (a) Proportion of 22 types of immune cells in the ALF group. (b) Correlations among seven PANoptosis-related genes and 22 immune cell types. (c) Comparison of the proportions of 22 kinds of immune cells between the ALF and control groups. * ***P*<0.05**; ** ***P*<0.01**; *** ***P*<0.001**; **** ***P*<0.0001.**

expression level gradually decreased, suggesting that it may be a protective protein. The expression of CASP1 also gradually decreased, but the amount of cleaved caspase-1 increased during the modeling.

Next, we explored the cellular localization of the seven target genes. According to the WB results, all seven genes were expressed 4 h after modeling, so we selected the liver sections sampled at that time point. As shown in the Fig. 8d, the expression of BMF and UNC5B was low in macrophages (golden arrow). BNIP3L and F4/80 expression overlapped almost completely, indicating that BNIP3L was expressed mainly in F4/80^{+} macrophages. There was good overlap between CASP1/RIPK3/UACA and CD11b, which confirmed that these three genes were expressed mainly in F4/80^{+}, CD11b^{+}, and Ly6C^{+} monocyte-derived macrophages (MoMFs). ZBP1 overlapped well with DAPI, indicating that ZBP1 is expressed mainly in the nucleus. The immunofluorescence results showed that macrophages expressed these seven genes, but the genes were not expressed only in macrophages.

Immune cells in the liver are mainly macrophages, and the results of immune infiltration showed that all seven molecules were closely associated with monocytes and macrophages. Therefore, we performed flow cytometric analysis on liver macrophages. We observed that Kupffer cells (KCs) showed a trend of an initial decrease followed by reduction, while peripheral monocytes showed a trend of initial increase followed by reduction, with both reaching their peak values at 1 h, indicating a complementary pattern (Figs. 9a and 9b; $P<0.05$).

To further confirm the reliability of the flow results, the liver sections were stained by immunofluorescence. We found that the number of macrophages of F4/80^{+} and CD11b^{+} decreased immediately within 0.5 h after LPS/D-gal stimulation, and then increased, reaching a peak at 6 h after LPS/D-gal stimulation. Ly6C^{+} macrophages also decreased within 0.5 h after LPS/D-gal stimulation, then increased slowly, reaching a peak at 4 h, and then decreased again at 6 h (Fig. 9c). Although the time point of the minimum value differs from that of the flow diagram, the general trend is consistent with the change shown by the flow results. In addition, we also measured the average fluorescence intensity (AVI) of Ly6C^{+} cells and found

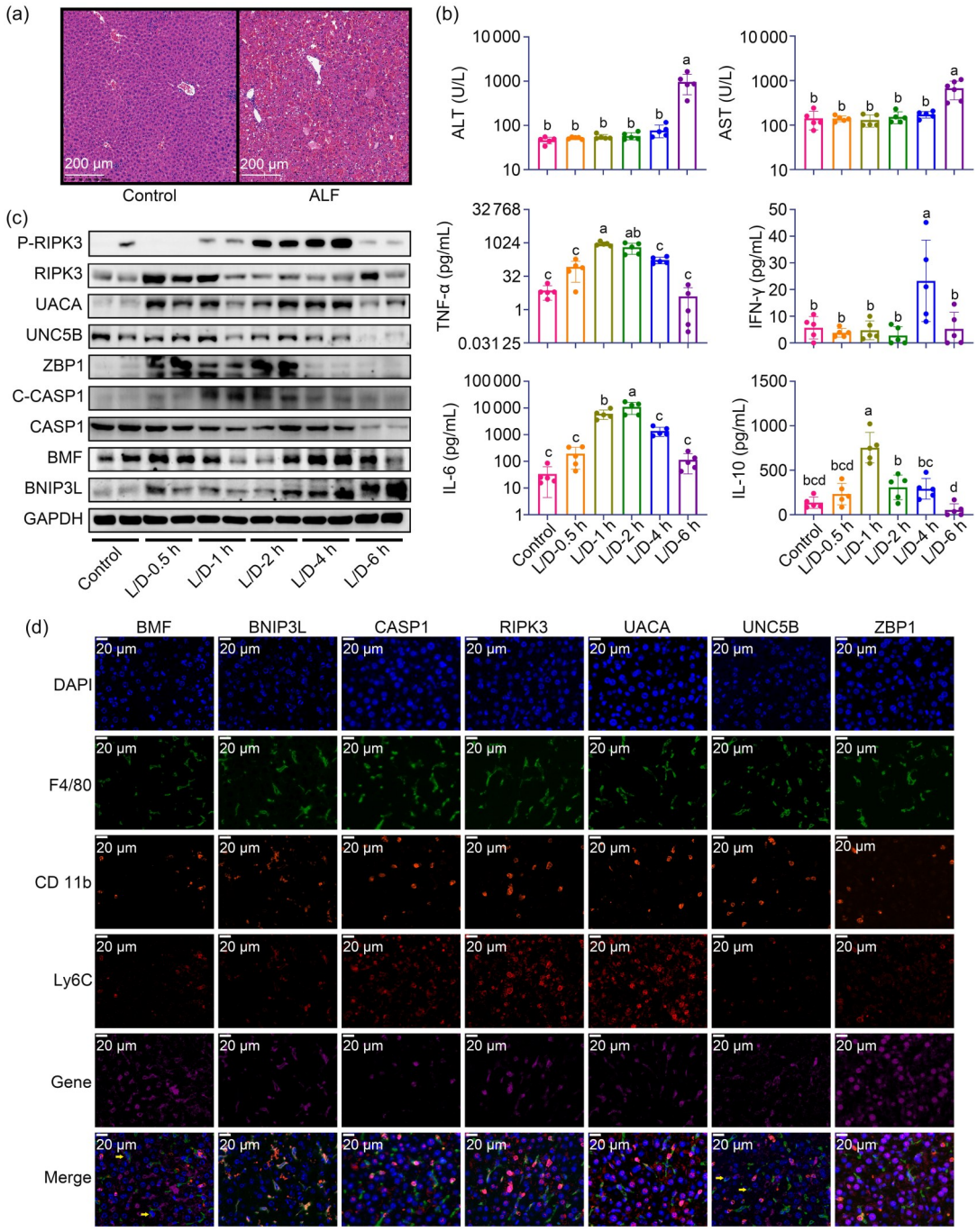

Fig. 8 Verification of the animal model. (a) Hematoxylin and eosin (H&E) staining of liver sections. (b) Levels of serum alanine aminotransferase (ALT), aspartate aminotransferase (AST), tumor necrosis factor-α (TNF-α), interferon-γ (IFN-γ), interleukin (IL)-6, and IL-10. (c) Changes of the expression levels of nine kinds of proteins with the time of modeling by western blot. (d) Cellular localization analyses of the seven genes through immunofluorescence with tyramide signal amplification (TSA). Data are expressed as mean±standard deviation (n=5). The presence of the same letter between two groups indicates no significant difference between them, and the absence of the same letter indicates a significant difference between them (P<0.05). The golden arrows indicate macrophages expressing BMF or UNC5B. BMF: B-cell lymphoma-2-modifying factor; BNIP3L: B-cell lymphoma-2-interacting protein 3-like; CASP1: Caspase-1; C-CASP1: cleaved CASP1; DAPI: 4',6-diamidino-2-phenylindole; GAPDH: glyceraldehyde-3-phosphate dehydrogenase; L/D: lipopolysaccharide/D-galactosamine; RIPK3: receptor-interacting protein kinase 3; P-RIPK3: phosphorylated RIPK3; UACA: uveal autoantigen with coiled-coil domains and ankyrin repeats protein; UNC5B: uncoordinated-5 homolog B receptor; ZBP1: Z-DNA-binding protein 1.

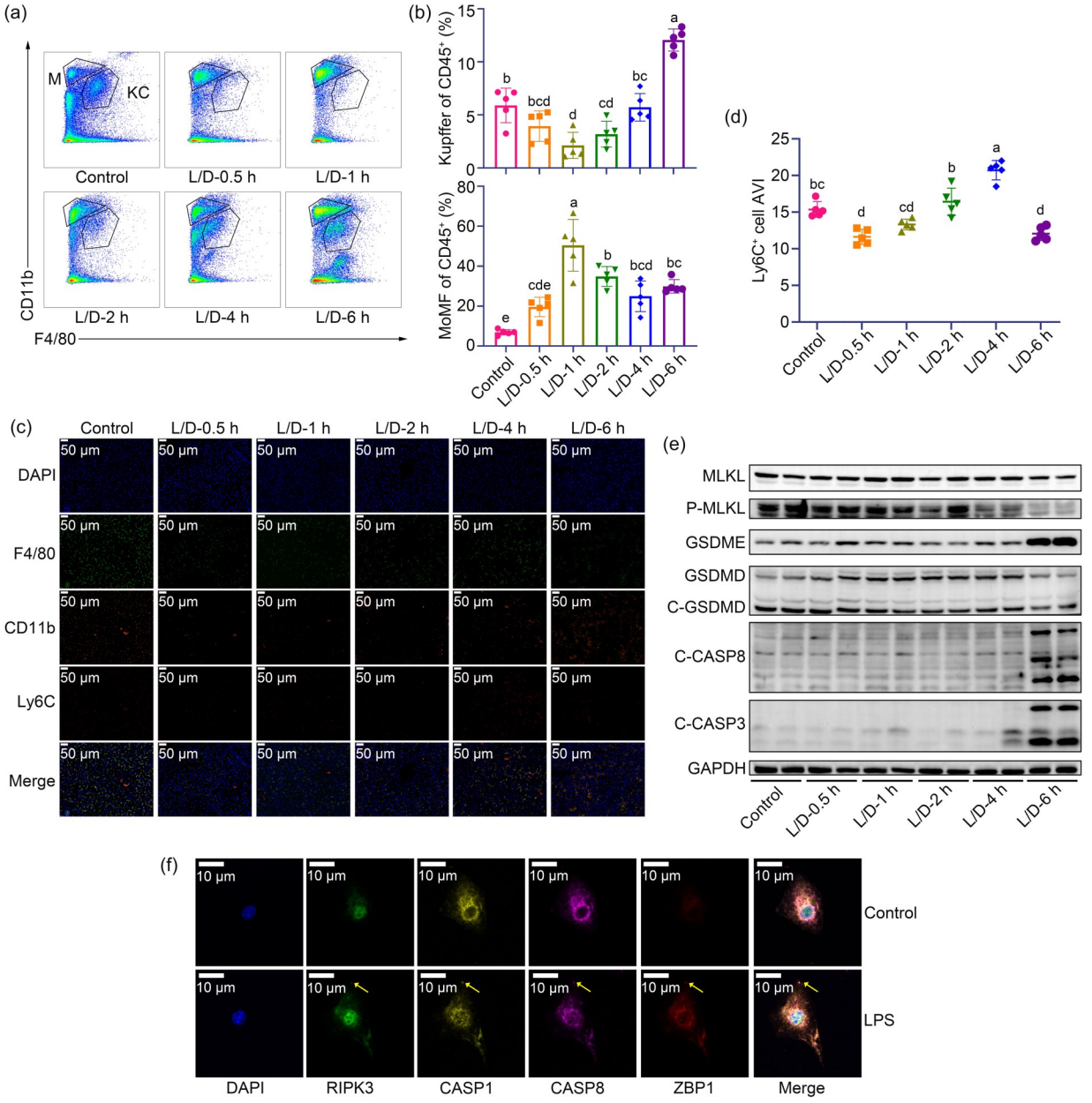

Fig. 9 Changes in macrophages, pyroptosis, apoptosis, and necroptosis in the liver after LPS/D-gal stimulation (labeled L/D). (a) Representative flow cytometry plots of Kupffer cells (labeled KC) and MoMFs (labeled M) of each group. (b) Percentages of Kupffer cells and MoMFs in hepatic CD45$^+$ cells. (c) Immunofluorescence results of macrophages in liver tissue at different time points after LPS/D-gal stimulation. (d) Average fluorescence intensity (AVI) of Ly6C$^+$ cells. (e) Trends of biomarkers of pyroptosis, apoptosis, and necroptosis. (f) Immunofluorescence results of PANoptosomes in bone marrow-derived macrophages (BMDMs) after LPS stimulation for 6 h (63× oil immersion objective). The golden arrows show the PANoptosome protein complex. Data are expressed as mean±standard deviation (n=5). The presence of the same letter between two groups indicates no significant difference between them, and the absence of the same letter indicates a significant difference between them (P<0.05). C-GSDMD: cleaved gasdermin D; C-CASP8: cleaved Caspase-8; C-CASP3: cleaved Caspase-3; DAPI: 4',6-diamidino-2-phenylindole; D-gal: D-galactosamine; LPS: lipopolysaccharide; MoMFs: monocyte-derived macrophages.

that it decreased after LPS/D-gal stimulation, then gradually increased, reaching a peak at 4 h, and then declined. Since MoMFs highly express Ly6C (Fig. 9d), this may indicate that the increased macrophages in the liver after LPS/D-gal stimulation are derived from peripheral monocytes.

As PANoptosis has the characteristics of pyroptosis, apoptosis, and necroptosis, we detected the markers of these three modes of cell death. The expression of MLKL decreased at 6 h after modeling, while the expression of its activation product P-MLKL was high before 2 h and then gradually decreased, indicating that necroptosis occurs mainly in the early stage of ALF. This result was basically consistent with that of P-RIPK3. GSDME expression increased significantly at 6 h after modeling, and cleaved GSDMD expression decreased immediately after stimulation with LPS/D-gal, indicating that the factor inducing pyroptosis gradually changed from GSDMD to GSDME with disease progression. Apoptotic markers, cleaved caspase-3 and cleaved caspase-8, were significantly increased at the end stage of liver failure, indicating that apoptosis was also present at the stage of liver failure (Fig. 9e). Both pyroptosis and apoptosis occur in the end stage of ALF, and all three modes of cell death are involved in the development of ALF. This shows that the cell death modes are not independent of each other, and further highlights the importance of PANoptosis in ALF.

Finally, PANoptosis is a process of cell death mediated by PANoptosomes. The detection of PANoptosomes is the gold standard for confirming the occurrence of PANoptosis. For this purpose, we isolated BMDMs from mice and constructed a cell model of ALF with LPS stimulation. Subsequently, PANoptosomes were detected by immunofluorescence combined with the TSA technique. We found that compared with the control group, PANoptosomes composed of ZBP1, RIPK3, CASP1, and CASP8 were formed in BMDM cells after LPS stimulation, as shown by the obvious overlapping of immunofluorescence of the four proteins observed under the microscope (Fig. 9f, golden arrows). This indicates that BMDMs undergo PANoptosis after LPS stimulation. Similar to BMDMs, MoMFs are also derived from bone marrow monocytes. Therefore, we believe that the PANoptosis of macrophages promotes the occurrence and development of ALF (Fig. 9f).

4 Discussion

In recent years, the combination of microarray and sequencing methods with integrative bioinformatics analysis has been increasingly used to investigate potential diagnostic biomarkers, underlying mechanisms, and prospective therapeutic targets of diseases (Petrik, 2006; Su et al., 2011).

Although there are numerous factors that can lead to ALF, the central common factor is the cytokine storm triggered by an immune response. Previously, the main focus was on studying the cytokine storm associated with specific types of cell death, such as pyroptosis, apoptosis, and necroptosis, overlooking the interconnections among the different forms of cell death (Duan et al., 2022; Huo et al., 2023; Li et al., 2023; Vasudevan et al., 2023). Hence, the identification of PANoptosis effectively addresses this gap. Presently, studies on PANoptosis concentrate mainly on cancer and corona virus disease 2019 (COVID-19) (Karki et al., 2021a, 2021b). As far as we know, this research represents the first exploration of the potential link between ALF and PANoptosis, potentially unveiling new targets for the future prevention, diagnosis, and treatment of ALF.

Despite the complex and diverse etiology of ALF, including factors such as infections, drug toxicity, and autoimmune reactions, immune reactions play a role in nearly all instances of the disease (Bernal and Wendon, 2013; Stravitz and Lee, 2019), with similarities observed in these immune reactions across different scenarios. Based on this foundation, in this study we integrated three ALF databases with distinct etiologies to yield more comprehensive findings. Initially, 5113 DEGs were identified from the combined dataset. Subsequently, we used the WGCNA method to categorize these genes functionally and identify gene modules with notable differences. Ultimately, we intersected these results with a gene set related to PANoptosis to identify seven key target genes. While obtaining the PANoptosis-related gene set, consensus had not been reached on genes associated with PANoptosis. Therefore, we assembled a PANoptosis-related gene set comprising 75 genes by merging genes involved in processes like pyroptosis, apoptosis, and necroptosis, along with genes involved in PANoptosis (Pan et al., 2022). The progression of ALF relies on the interactions of genes. As indicated by the violin plot, the expression of the seven feature genes was consistently higher in the ALF group than in the control group, underscoring their pivotal roles in the pathophysiology of ALF.

Early biochemical analyses showed that BMF was associated with actin filaments in the cytoskeleton.

Under certain cellular stress conditions, BMF can change subcellular localization, and then transfer into mitochondria and co-immunoprecipitate with B-cell lymphoma 2 (Bcl2) to trigger apoptosis, which may be mediated by the TGF-β signaling pathway through the activation of Runt-related transcription factor 3 (RUNX3) (Puthalakath et al., 2001; Puthalakath and Strasser, 2002; Yamamura et al., 2006; Ramjaun et al., 2007). Early studies indicated that a hypoxic environment stimulates the up-regulation of BNIP3L via hypoxia-inducible factor 1 (HIF-1), and subsequent research has confirmed that BNIP3L can trigger mitophagy (Sowter et al., 2001; Chen et al., 2023; Verbeke et al., 2023). In advanced stages of ALF, impaired coagulation function can lead to tissue hypoxia, resulting in increased expression of BNIP3L. Furthermore, WB analysis of mouse tissues shows that after 6 h of modeling, severe liver congestion is evident, with peak BNIP3L expression observed at this stage. Perhaps inhibiting BNIP3L could alleviate the progression of ALF, or BNIP3L could serve as a predictive molecule. Currently, research on CASP1 focuses mainly on two aspects: the CASP1-dependent canonical pyroptosis pathway, and the NLR family, pyrin domain-containing 3 (NLRP3)/CASP1 inflammasome pathway (Wang et al., 2017; Yu et al., 2023). Our WB results in this study indicate a decrease in CASP1 expression levels in the late stages of modeling, while the expression level of the activated type of cleaved caspase-1 increased. These changes are possibly attributed to the pronounced liver congestion and hypoxic conditions prevalent in the tissue at this stage of modeling. This observation is consistent with past studies indicating that HIF-1 can activate the NLRP3/CASP1 signaling pathway (Jiang et al., 2022). In vitro experiments also showed a correlation between hypoxia and the NLRP3/apoptosis-associated speck-like protein containing a caspase recruitment domain (ASC)/CASP1 signaling axis (Slowik et al., 2018). RIPK1/RIPK3/MLKL constitutes the core of the necroptosis signaling pathway. Upon activation of Toll-like receptor 4 (TLR4) by LPS, RIPK1 is indirectly recruited through TIR-domain-containing adapter-inducing IFN-β (TRIF). Accompanied by the inhibition of CASP8 activity, RIPK3 is activated and recruits MLKL later. Phosphorylation of MLKL by RIPK3 leads to its translocation to the cell membrane, ultimately resulting in cell rupture (Newton, 2015). Research indicates that RIPK1 and RIPK3 can activate the NLRP3 inflammasome and contribute to autoimmune diseases (Speir and Lawlor, 2021). Our WB results showed that RIPK3 is activated within just 0.5 h after modeling, suggesting that necroptosis is the earliest form of cell death. Monitoring markers associated with necroptosis could potentially act as a valuable early detection tool. UACA could interact with apoptotic protease-activating factor-1 (Apaf-1) and translocate it into the nucleus under proapoptotic stress to induce apoptosis (Sakai et al., 2003; Ohkura et al., 2004). Also, UACA interacted with the nuclear factor-κB (NF-κB) to reduce the expression of the NF-κB-targeted genes (Liu et al., 2009). In this study, the expression level of UACA consistently increased during the modeling process and decreased towards the later stages. We believe that the initial increase in expression is aimed mainly at inducing apoptosis, while the subsequent decrease in expression is intended to enhance the expression of NF-κB-targeted genes. The UNC5B signaling pathway involves monocyte differentiation into macrophages, macrophage infiltration, angiogenesis, cell apoptosis, and endoplasmic reticulum stress (Koch et al., 2011; Choi et al., 2022; Huang et al., 2022; Fang et al., 2023; Yang et al., 2023). Research suggests that the absence of UNC5B exacerbates tissue injury in acute kidney injury. In our research, we observed a decrease in UNC5B expression as the modeling time prolonged, confirming its protective function. This trend was also supported by the flow cytometry results. The initial increase followed by a decrease in peripheral monocytes is attributed to the reduction in UNC5B expression in the early stages of modeling being insufficient to prevent the recruitment and differentiation of peripheral monocytes, whereas the subsequent decrease is due to insufficient UNC5B. The later decrease in peripheral monocytes is due to insufficient UNC5B levels. Similarly, the initial decrease and subsequent increase in KCs are a result of MoMFs acquiring a KC-like phenotype after acute or specific KC depletion under various signaling influences (Guillot and Tacke, 2023). ZBP1 is a crucial initiator of both innate immune responses and PANoptosis. Its activation of innate immune responses includes type I IFN response and NF-κB signaling, forming a critical defense line against pathogenic infections. ZBP1-mediated PANoptosis presents a double-edged sword: it can eliminate infected cells and tumor cells, but excessive PANoptosis can trigger a cytokine storm and pose

harm to the host. Our WB results also showed that ZBP1 expression increased in the initial phases of modeling, further confirming its role as an initiator (Takaoka et al., 2007; Rebsamen et al., 2009; Hao et al., 2022). Subsequently, we conducted an analysis of the cellular localization of seven genes via immunofluorescence. Results showed that macrophages can express these seven genes. Next, we investigated the markers of pyroptosis, apoptosis, and necroptosis, revealing that the three types of RCD are intertwined throughout the progression of ALF, which further emphasizes the importance of PANoptosis in ALF. Finally, using the cell model of ALF, we confirmed that macrophages could form PANoptosomes to induce PANoptosis.

This study, encompassing database analysis and animal studies, highlights the pivotal role of PANoptosis in the onset and progression of ALF. However, it had several limitations. Firstly, the data were obtained from public databases, which imposed limitations on sample size. Secondly, the lack of consensus on PANoptosis-related genes may result in certain omissions. Thirdly, although we validated the expression of relevant genes in the mouse liver, their underlying mechanisms have not been further verified. Lastly, the challenge of acquiring clinical ALF samples prevented us from obtaining further validation from patients. Nevertheless, our study has provided valuable and novel insights.

5 Conclusions

Our study revealed new insights into the development and progression of ALF using advanced bioinformatics techniques. We successfully identified and confirmed the roles of seven PANoptosis-related genes, and validated the involvement of macrophages in this process. This discovery has the potential to significantly impact the development of diagnostic markers and treatment strategies for ALF, as we gain a deeper understanding of its molecular mechanisms.

Data availability statement

The dataset used or analyzed during the current study is available from the corresponding author on reasonable request.

Acknowledgments

This work was supported by the National Science and Technology Major Project of China (No. 2018ZX10302206).

Author contributions

Zhi CHEN and Junwei SHAO contributed to the study conception and design, and revising the final version of the manuscript. Tiantian GE and Yao CHEN contributed to the data collection, assembly, analysis, interpretation, and the manuscript drafting. Tiantian GE and Lantian PANG contributed to the animal experiment. All authors have read and approved the final manuscript, and therefore, have full access to all the data in the study and take responsibility for the integrity and security of the data.

Compliance with ethics guidelines

Zhi CHEN is an Editorial Board Member for *Journal of Zhejiang University-SCIENCE B (Biomedicine & Biotechnology)* and was not involved in the editorial review or the decision to publish this article. Tiantian GE, Yao CHEN, Lantian PANG, Junwei SHAO, and Zhi CHEN declare that they have no conflicts of interest.

The animal experiments adhered to the ethical principles outlined in the Declaration of Helsinki and received approval from the research ethics committee of the First Affiliated Hospital of Zhejiang University School of Medicine (No. 20211404).

References

Bernal W, Wendon J, 2013. Acute liver failure. *N Engl J Med*, 369(26):2525-2534. https://doi.org/10.1056/NEJMra1208937

Chen YJ, Jiao DY, Liu Y, et al., 2023. FBXL4 mutations cause excessive mitophagy via BNIP3/BNIP3L accumulation leading to mitochondrial DNA depletion syndrome. *Cell Death Differ*, 30(10):2351-2363. https://doi.org/10.1038/s41418-023-01205-1

Choi SW, Oh H, Park SY, et al., 2022. Netrin-1 attenuates hepatic steatosis *via* UNC5b/PPARγ-mediated suppression of inflammation and ER stress. *Life Sci*, 311:121149. https://doi.org/10.1016/j.lfs.2022.121149

Christgen S, Zheng M, Kesavardhana S, et al., 2020. Identification of the panoptosome: a molecular platform triggering pyroptosis, apoptosis, and necroptosis (panoptosis). *Front Cell Infect Microbiol*, 10:237. https://doi.org/10.3389/fcimb.2020.00237

Duan YW, Chen SX, Li QY, et al., 2022. Neuroimmune mechanisms underlying neuropathic pain: the potential role of TNF-α-necroptosis pathway. *Int J Mol Sci*, 23(13):7191. https://doi.org/10.3390/ijms23137191

Fang YX, Ma KY, Huang YM, et al., 2023. Fibronectin leucine-rich transmembrane protein 2 drives monocyte differentiation into macrophages *via* the UNC5B-Akt/mTOR axis. *Front Immunol*, 14:1162004. https://doi.org/10.3389/fimmu.2023.1162004

Galluzzi L, Kepp O, Krautwald S, et al., 2014. Molecular mechanisms of regulated necrosis. *Semin Cell Dev Biol*, 35:24-32. https://doi.org/10.1016/j.semcdb.2014.02.006

Galluzzi L, Bravo-San Pedro JM, Vitale I, et al., 2015. Essential *versus* accessory aspects of cell death: recommendations of the NCCD 2015. *Cell Death Differ*, 22(1):58-73. https://doi.org/10.1038/cdd.2014.137

Green DR, Kroemer G, 2005. Pharmacological manipulation of cell death: clinical applications in sight? *J Clin Invest*, 115(10):2610-2617. https://doi.org/10.1172/JCI26321

Guillot A, Tacke F, 2023. Spatial dimension of macrophage heterogeneity in liver diseases. *eGastroenterology*, 1(1): e000003. https://doi.org/10.1136/egastro-2023-000003

Hao Y, Yang B, Yang JK, et al., 2022. ZBP1: a powerful innate immune sensor and double-edged sword in host immunity. *Int J Mol Sci*, 23(18):10224. https://doi.org/10.3390/ijms231810224

Huang L, An XZ, Zhu Y, et al., 2022. Netrin-1 induces the anti-apoptotic and pro-survival effects of B-ALL cells through the Unc5b-MAPK axis. *Cell Commun Signal*, 20: 122. https://doi.org/10.1186/s12964-022-00935-y

Huo CY, Tang YL, Li XS, et al., 2023. Melatonin alleviates lung injury in H1N1-infected mice by mast cell inactivation and cytokine storm suppression. *PLoS Pathog*, 19(5): e1011406. https://doi.org/10.1371/journal.ppat.1011406

Jiang WK, Sun SK, Wang DY, et al., 2022. MicroRNA-22 suppresses NLRP3/CASP1 inflammasome pathway-mediated proinflammatory cytokine production by targeting the HIF-1α and NLRP3 in human dental pulp fibroblasts. *Int Endod J*, 55(11):1225-1240. https://doi.org/10.1111/iej.13814

Karki R, Sundaram B, Sharma BR, et al., 2021a. ADAR1 restricts ZBP1-mediated immune response and PANoptosis to promote tumorigenesis. *Cell Rep*, 37(3):109858. https://doi.org/10.1016/j.celrep.2021.109858

Karki R, Sharma BR, Tuladhar S, et al., 2021b. Synergism of TNF-α and IFN-γ triggers inflammatory cell death, tissue damage, and mortality in SARS-CoV-2 infection and cytokine shock syndromes. *Cell*, 184(1):149-168.e17. https://doi.org/10.1016/j.cell.2020.11.025

Khan SA, Shah N, Williams R, et al., 2006. Acute liver failure: a review. *Clin Liver Dis*, 10(2):239-258. https://doi.org/10.1016/j.cld.2006.05.010

Koch AW, Mathivet T, Larrivée B, et al., 2011. Robo4 maintains vessel integrity and inhibits angiogenesis by interacting with UNC5B. *Dev Cell*, 20(1):33-46. https://doi.org/10.1016/j.devcel.2010.12.001

Kuriakose T, Man SM, Subbarao Malireddi RK, et al., 2016. ZBP1/DAI is an innate sensor of influenza virus triggering the NLRP3 inflammasome and programmed cell death pathways. *Sci Immunol*, 1(2):aag2045. https://doi.org/10.1126/sciimmunol.aag2045

Leek JT, Johnson WE, Parker HS, et al., 2012. The sva package for removing batch effects and other unwanted variation in high-throughput experiments. *Bioinformatics*, 28(6): 882-883. https://doi.org/10.1093/bioinformatics/bts034

Li AC, Yang Q, Lou GH, et al., 2021. 5-((7-Chloro-6-fluoro-1h-indol-3-yl) methyl)-3-methylimidazolidine-2,4-dione as a RIP1 inhibitor protects LPS/D-galactosamine-induced liver failure. *Life Sci*, 273:119304. https://doi.org/10.1016/j.lfs.2021.119304

Li XX, Li XC, Yang JL, et al., 2023. In situ sustained macrophage-targeted nanomicelle-hydrogel microspheres for inhibiting osteoarthritis. *Research (Wash D C)*, 6:0131. https://doi.org/10.34133/research.0131

Lin JF, Hu PS, Wang YY, et al., 2022. Phosphorylated NFS1 weakens oxaliplatin-based chemosensitivity of colorectal cancer by preventing panoptosis. *Signal Transduct Target Ther*, 7:54. https://doi.org/10.1038/s41392-022-00889-0

Liu L, Sakai T, Tran NH, et al., 2009. Nucling interacts with nuclear factor-κB, regulating its cellular distribution. *FEBS J*, 276(5):1459-1470. https://doi.org/10.1111/j.1742-4658.2009.06888.x

Long JS, Ryan KM, 2012. New frontiers in promoting tumour cell death: targeting apoptosis, necroptosis and autophagy. *Oncogene*, 31(49):5045-5060. https://doi.org/10.1038/onc.2012.7

Malireddi RKS, Gurung P, Mavuluri J, et al., 2018. TAK1 restricts spontaneous NLRP3 activation and cell death to control myeloid proliferation. *J Exp Med*, 215(4):1023-1034. https://doi.org/10.1084/jem.20171922

Malireddi RKS, Kesavardhana S, Kanneganti TD, 2019. ZBP1 and TAK1: master regulators of NLRP3 inflammasome/pyroptosis, apoptosis, and necroptosis (PAN-optosis). *Front Cell Infect Microbiol*, 9:406. https://doi.org/10.3389/fcimb.2019.00406

Newton K, 2015. RIPK1 and RIPK3: critical regulators of inflammation and cell death. *Trends Cell Biol*, 25(6):347-353. https://doi.org/10.1016/j.tcb.2015.01.001

Nguyen LN, Kanneganti TD, 2022. PANoptosis in viral infection: the missing puzzle piece in the cell death field. *J Mol Biol*, 434(4):167249. https://doi.org/10.1016/j.jmb.2021.167249

Ohkura T, Taniguchi SI, Yamada K, et al., 2004. Detection of the novel autoantibody (anti-UACA antibody) in patients with Graves' disease. *Biochem Biophys Res Commun*, 321(2):432-440. https://doi.org/10.1016/j.bbrc.2004.06.162

Pan HD, Pan JX, Li P, et al., 2022. Characterization of PANoptosis patterns predicts survival and immunotherapy response in gastric cancer. *Clin Immunol*, 238:109019. https://doi.org/10.1016/j.clim.2022.109019

Petrik J, 2006. Diagnostic applications of microarrays. *Transfus Med*, 16(4):233-247. https://doi.org/10.1111/j.1365-3148.2006.00673.x

Puthalakath H, Strasser A, 2002. Keeping killers on a tight leash: transcriptional and post-translational control of the pro-apoptotic activity of BH3-only proteins. *Cell Death Differ*, 9(5):505-512.

https://doi.org/10.1038/sj.cdd.4400998

Puthalakath H, Villunger A, O'Reilly LA, et al., 2001. Bmf: a proapoptotic BH3-only protein regulated by interaction with the myosin V actin motor complex, activated by anoikis. *Science*, 293(5536):1829-1832. https://doi.org/10.1126/science.1062257

Ramjaun AR, Tomlinson S, Eddaoudi A, et al., 2007. Upregulation of two BH3-only proteins, Bmf and Bim, during TGF*β*-induced apoptosis. *Oncogene*, 26(7):970-981. https://doi.org/10.1038/sj.onc.1209852

Rebsamen M, Heinz LX, Meylan E, et al., 2009. DAI/ZBP1 recruits RIP1 and RIP3 through RIP homotypic interaction motifs to activate NF-κB. *EMBO Rep*, 10(8):916-922. https://doi.org/10.1038/embor.2009.109

Sakai T, Liu L, Shishido Y, et al., 2003. Identification of a novel, embryonal carcinoma cell-associated molecule, nucling, that is up-regulated during cardiac muscle differentiation. *J Biochem*, 133(4):429-436. https://doi.org/10.1093/jb/mvg056

Schwabe RF, Luedde T, 2018. Apoptosis and necroptosis in the liver: a matter of life and death. *Nat Rev Gastroenterol Hepatol*, 15(12):738-752. https://doi.org/10.1038/s41575-018-0065-y

Slowik A, Lammerding L, Zendedel A, et al., 2018. Impact of steroid hormones E2 and P on the NLRP3/ASC/Casp1 axis in primary mouse astroglia and BV-2 cells after in vitro hypoxia. *J Steroid Biochem Mol Biol*, 183:18-26. https://doi.org/10.1016/j.jsbmb.2018.05.003

Sowter HM, Ratcliffe PJ, Watson P, et al., 2001. HIF-1-dependent regulation of hypoxic induction of the cell death factors BNIP3 and NIX in human tumors. *Cancer Res*, 61(18):6669-6673.

Speir M, Lawlor KE, 2021. RIP-roaring inflammation: RIPK1 and RIPK3 driven NLRP3 inflammasome activation and autoinflammatory disease. *Semin Cell Dev Biol*, 109:114-124. https://doi.org/10.1016/j.semcdb.2020.07.011

Stravitz RT, Lee WM, 2019. Acute liver failure. *Lancet*, 394(10201):869-881. https://doi.org/10.1016/S0140-6736(19)31894-X

Su ZQ, Ning BT, Fang H, et al., 2011. Next-generation sequencing and its applications in molecular diagnostics. *Expert Rev Mol Diagn*, 11(3):333-343. https://doi.org/10.1586/erm.11.3

Takaoka A, Wang ZC, Choi MK, et al., 2007. DAI (DLM-1/ZBP1) is a cytosolic DNA sensor and an activator of innate immune response. *Nature*, 448(7152):501-505. https://doi.org/10.1038/nature06013

Vasudevan SO, Behl B, Rathinam VA, 2023. Pyroptosis-induced inflammation and tissue damage. *Semin Immunol*, 69:101781. https://doi.org/10.1016/j.smim.2023.101781

Verbeke J, de Bolle X, Arnould T, 2023. When mitophagy dictates the outcome of cellular infection: the case of *Brucella abortus*. *Autophagy*, 19(11):3022-3023. https://doi.org/10.1080/15548627.2023.2246354

Wang DY, Zhang JB, Jiang WK, et al., 2017. The role of NLRP3-CASP1 in inflammasome-mediated neuroinflammation and autophagy dysfunction in manganese-induced, hippocampal-dependent impairment of learning and memory ability. *Autophagy*, 13(5):914-927. https://doi.org/10.1080/15548627.2017.1293766

Wang Y, Chen Q, Jiao FZ, et al., 2021. Histone deacetylase 2 regulates ULK1 mediated pyroptosis during acute liver failure by the K68 acetylation site. *Cell Death Dis*, 12:55. https://doi.org/10.1038/s41419-020-03317-9

Yamamura Y, Lee WL, Inoue K, et al., 2006. RUNX3 cooperates with FoxO3a to induce apoptosis in gastric cancer cells. *J Biol Chem*, 281(8):5267-5276. https://doi.org/10.1074/jbc.M512151200

Yan WT, Zhao WJ, Hu XM, et al., 2023. PANoptosis-like cell death in ischemia/reperfusion injury of retinal neurons. *Neural Regen Res*, 18(2):357-363. https://doi.org/10.4103/1673-5374.346545

Yang X, Ma LM, Zhang J, et al., 2023. Hypofucosylation of Unc5b regulated by Fut8 enhances macrophage emigration and prevents atherosclerosis. *Cell Biosci*, 13:13. https://doi.org/10.1186/s13578-023-00959-y

Yu XB, Liu X, Liu X, et al., 2023. Overexpression of CASP1 triggers acute promyelocytic leukemia cell pyroptosis and differentiation. *Eur J Pharmacol*, 945:175614. https://doi.org/10.1016/j.ejphar.2023.175614

Zheng YF, Sun WR, Shan C, et al., 2022. β-Hydroxybutyrate inhibits ferroptosis-mediated pancreatic damage in acute liver failure through the increase of H3K9bhb. *Cell Rep*, 41(12):111847. https://doi.org/10.1016/j.celrep.2022.111847